applied sciences

MDPI

Article

Hysteresis Measurements and Numerical Losses Segregation of Additively Manufactured Silicon Steel for 3D Printing Electrical Machines

Hans Tiismus [1,*], Ants Kallaste [1], Anouar Belahcen [2], Toomas Vaimann [1,3], Anton Rassõlkin [1,3] and Dmitry Lukichev [3]

[1] Institute of Electrical Power Engineering and Mechatronics, Tallinn University of Technology, 19086 Tallinn, Estonia; ants.kallaste@taltech.ee (A.K.); toomas.vaimann@taltech.ee (T.V.); anton.rassolkin@taltech.ee (A.R.)

[2] Department of Electrical Engineering and Automation, Aalto University, 02150 Espoo, Finland; Anouar.Belahcen@aalto.fi

[3] Faculty of Control Systems and Robotics, ITMO University, Saint Petersburg 197101, Russia; lukichev@itmo.ru

* Correspondence: hans.tiismus@taltech.ee; Tel.: +37-2-5335-8327

Received: 1 September 2020; Accepted: 15 September 2020; Published: 18 September 2020

check for updates

Abstract: Samples from FeSi4 powder were fabricated with a low power selective laser melting (SLM) system using a laser re-melting strategy. The sample material was characterized through magnetic measurements. The study showed excellent DC magnetic properties, comparable to commercial and other 3D printed soft ferromagnetic materials from the literature at low (1 T) magnetization. Empirical total core losses were segregated into hysteresis, eddy and excessive losses via the subtraction of finite element method (FEM) simulated eddy current losses and hysteresis losses measured at quasi-static conditions. Hysteresis losses were found to decrease from 3.65 to 0.95 W/kg (1 T, 50 Hz) after the annealing. Both empirical and FEM results confirm considerable eddy currents generated in the printed bulk toroidal sample, which increase dramatically at high material saturation after annealing. These losses could potentially be reduced by using partitioned material internal structure realized by printed airgaps. Similarly, with regard to the samples characterized in this study, the substantially increased core losses induced by material oversaturation due to reduced filling factor may present a challenge in realizing 3D printed electrical machines with comparable performance to established 2D laminated designs.

Keywords: electric machines; additive manufacturing; soft magnetic materials; selective laser melting; iron losses; FEM

1. Introduction

The ever-accelerating advancements in the capabilities, accessibilities and cost-efficiency of metal additive manufacturing (AM) platforms have sparked an interest in the electrical machine research community for developing novel three-dimensional topology-optimized 3D printed electrical machines (EM). As of yet, no research group has printed an EM with improved performance or efficiency over the traditionally manufactured EMs. In fact, fully 3D printing an EM without any assembly or post-processing during or after printing has yet to be achieved, however all the necessary components have successfully been individually fabricated: soft magnetic rotor [1,2] and stator designs [3], gapped [4] and insulated [5] coils and metal bearings [6]. For prototyping full 3D printing electrical machines, several hybrid methods have been employed that utilize additively manufactured components, such as inserting components during printing (bearings, coils and magnets) [7] or assembling components fabricated with dedicated metal printing systems after post-production [3].

Selective Laser Melting (SLM) printing systems have proven very capable in the creation of functional metallic parts and find employment for rapid prototyping and limited production of highly specialized parts for aerospace, automotive and astronautic sectors, where performance and mass reduction capabilities are important [8]. SLM systems are also the most widely adopted by the EM research community in the research and development of 3D printed EMs. Three distinct materials are required to be printed in parallel to successfully fabricate an EM: a diamagnetic material with high electrical conductivity (coils), ferromagnetic material with low electrical conductivity (core) and a diamagnetic / dielectric material (insulation). SLM fabrication of conductive (Cu [9], AlSi10Mg [10]) and soft ferromagnetic (FeSi6.7 [11], FeSi6.9 [12], FeSi3 [13], Fe-Co-V [14], Fe-Ni-Si [15]) materials has successfully been accomplished, however the technology has not been used for printing insulating materials concurrently with metallic materials. The lack of insulating materials in the SLM printed soft magnetic materials has no influence on applications with a quasi-static magnetic field, such as magnetic couplers or rotors of synchronous machines. However, it is inadequate for employment in EM stator constructions, due to the extensive eddy current generated in the non-laminated structure by the rotating magnetic fields, resulting in reduced efficiency and excessive thermal heating of the machine. Employing the spatial accuracy of additive manufacturing systems, finite internal material structures with geometrical manipulation can be achieved, which have been shown to reduce the classical eddy current generation considerably [11,13]. Introducing airgaps to the material, however, also reduces the material filling factor, which would require oversaturation to produce the same flux as in a fully dense or laminated structure.

This paper describes the sample preparation, printing, test setup and empirical results for magnetic measurements of SLM-fabricated soft ferromagnetic silicon steel. The material properties measured are applicable for modelling novel core geometries and are a starting point for optimizing the material internal structure for reduced core losses.

2. Materials and Methods

2.1. Printing System

All samples were prepared on SLM Solutions GmbH Realizer SLM-50 machine. It is a small, lab-scale printing system, with a circular build envelope and an axial re-coater arm with two wiper blades. The printer contains a 1070 nm yttrium scanning laser with a maximum power of 120 W, build envelope of D70 × H75 mm and enables pre-heating capacity of up to 200 °C. Printing can be conducted in inert argon or nitrogen gas environments, with oxygen content purged below 0.4% during the process. The schematic of the SLM-50 printing system is shown in Figure 1.

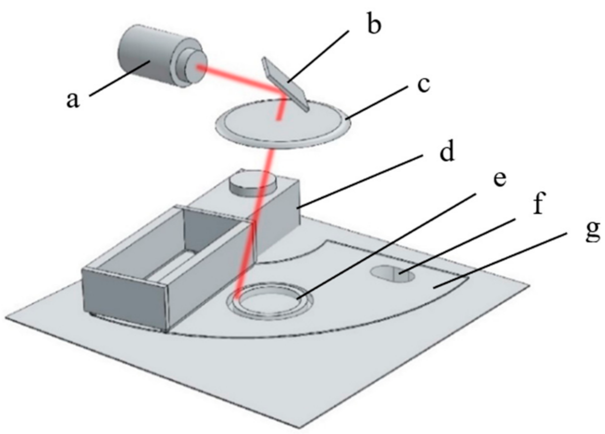

Figure 1. Realizer-50 selective laser melting (SLM) printing system: (**a**) laser, (**b**) scanning mirrors, (**c**) protective glass, (**d**) re-coater arm, (**e**) build platform with printed toroid sample, (**f**) powder supply opening, (**g**) powder coating.

2.2. Powder Characterization

The powder for the experiment was analyzed for the particle shape, size and chemical composition. In the study, commercially available gas-atomized pre-alloyed powder of Fe-Si was used. Table 1 shows the chemical composition of the experimental iron alloy powder.

Table 1. Summary of powder characterization.

Elements	Fe	Si	Cr
Wt %	Balance	4	1.3

The shape of powder particles was confirmed with scanning electron microscopy (SEM) to be roughly spherical, as shown in Figure 2a. Energy-dispersive X-ray spectroscope (EDX) integrated into the SEM system revealed average silicon content in the powder of 3.8–4.11% and 1.14–1.37% of chromium content. Chromium content in Fe-Si can be related to slightly lower magnetic saturation magnetization [16,17] of the material. The powder size distribution was determined with a laser scattering particle size distribution analyzer in a water dispersive environment. The median particle size was measured as 33.5 μm with a standard deviation of 7.8 μm, with the distribution shown in Figure 2b.

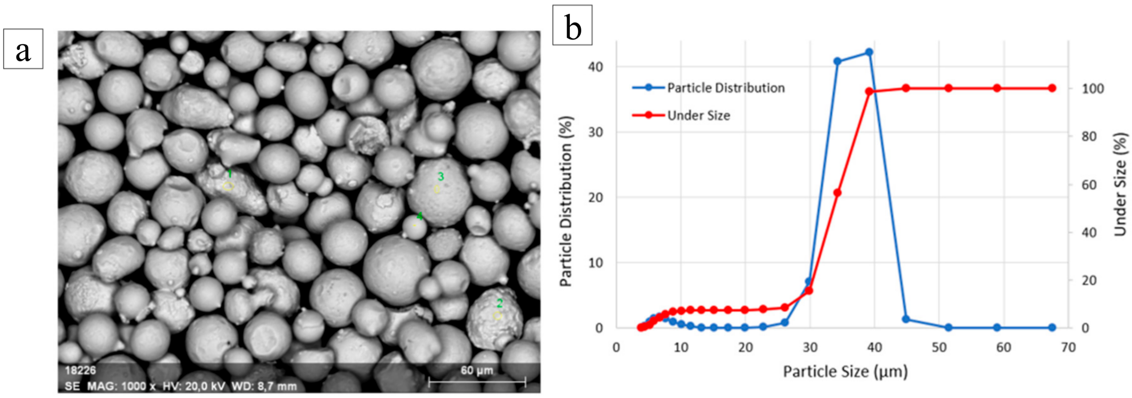

Figure 2. (**a**) Scanning electron microscope (SEM) magnification of the investigated powder, (**b**) Powder particle size distribution and percentage of particles below a specific particle size.

2.3. Printing Parameters

Prior to printing of the samples for magnetic measurements, printing parameters were determined for printing bulk samples from the Fe-Si-Cr powder with low porosity (up to 2%) and no visible macroscopic defects (visible cracks, delaminations or uneven growth). Default printing parameters of stainless steel 316 L for the Realizer SLM-50 printer were chosen as initial values of printing parameters (Table 2), resulting in printed samples with high porosity and macroscopic cracking. Next, a laser re-melting strategy was adopted for improving the printer material quality, as it enables the incremental melting of the powder: laser re-melting involves scanning each layer or the surface of the printed material twice, before applying the next layer of fresh power on the bed. Several studies have demonstrated improved density and surface quality with the strategy for SLM [18–20]. Printing of cubical 8 × 8 × 8 mm samples was performed to investigate different combinations of laser power and scanning speed on both the primary and secondary scans, layer thickness and hatch distance were constant throughout the study. The parameters of the study were limited to 50–75 W/75–100 W (primary/secondary scan) for the laser power and 1 m/s/0.5–2 m/s for the scanning velocity. Higher energy input (resulting in higher laser power or lower scanning velocity) was not investigated as it resulted in extensive sputtering (primary scan) or macroscopic cracking. The printing parameters employed for achieving the highest relative density of 98% with the least cracking are presented in Table 2 alongside the initial parameters. The structure of the printed samples was evaluated with standard metallographic practices with polishing and optical microscopy. The porosity was determined from the processing of thresholded images. The average sample absolute density of 7340 kg/m^3 was measured with the Archimedes scale method. Next, toroidal samples exhibiting a rectangular cross section of 5 × 5 mm, inner diameter of 50 mm and outer diameter of 60 mm were printed for magnetic measurements as shown on Figure 3a–c.

Table 2. Summary of the printing parameters.

Parameter	Inital	Final
Layer thickness	35 µm	35 µm
Hatch distance	60 µm	60 µm
Laser Power	75 W	50 W/75 W
Scanning velocity	1 m/s	1 m/s/0.75 m/s
Laser spot size	~100 µm	~100 µm
Pre-Heating	0 °C	200 °C
Environment	Argon	Argon
Oxygen content	~0.35%	~0.35%

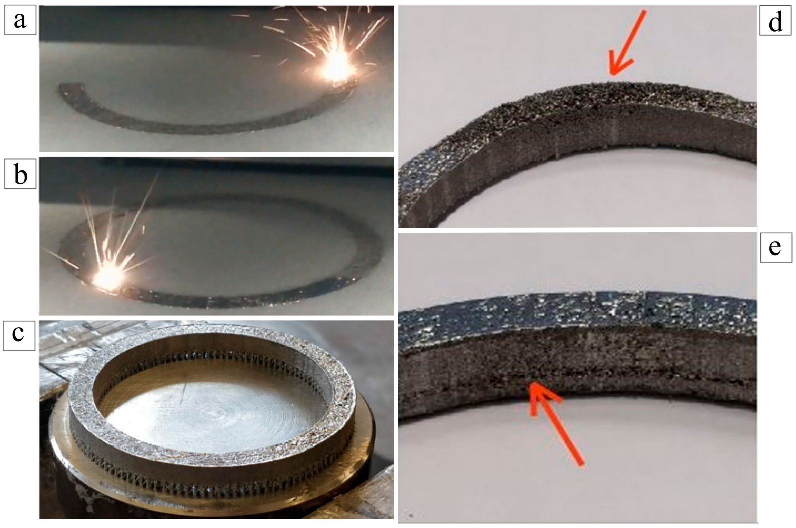

Figure 3. Laser re-melting process of the toroidal samples: (**a**) primary scan, (**b**) secondary scan, (**c**) finished toroid on stainless steel baseplate. (**d**) Toroid printed with uneven growth, (**e**) toroid printed with a delaminated layer.

Two powder coating related issues were met when advancing from cubical to toroidal samples:

- Uneven growth (Figure 3d)—due powder balling, the uneven growth resulted in inferior density of the printed part, distorted part dimensions and printing termination, if growth is prominent enough to restrict the re-coater movements. Uneven powder deposition on the part was determined as the main cause for this issue, which was solved by double re-coater swiping to brush away the excess powder. Even growth of the printed part also seemed to be promoted by the laser re-melting strategy, as incremental melting of each layer seemed helpful for eliminating emerging irregularities; and
- Delaminations (Figure 3e)—were the result of excessive powder deposition on the printed part. It occurred when operating the printer without a feeder mechanism (suitable for parts with low height) and adding powder to the build chamber manually during an interrupt in the printing process. In that case, the build platform needed to be raised slightly manually after adding the extra powder, until only a thin coating of powder is visible on the printed part.

2.4. Sample Annealing and Crystal Structure

Annealing of the toroid was performed for obtaining improved magnetic properties. The process was performed in a graphite chamber furnace on the account of the ready availability of this facility for this study. The toroid was heated up in vacuum environment (~0.1 mBar) to 1150 °C with a heating rate of 300 K/h, kept at the target temperature for 1 h and then slowly oven-cooled. The annealing parameters were chosen as optimal parameters described in the study by Garibaldi [12]. Due to potential carbon absorption during the annealing process in the graphite chamber furnace, Atomic Emission Spectroscopy (AES) analysis of the carbon content in the printed material was conducted both before and after annealing. The spectroscopy was performed on the surface of the samples, with three tests for both one annealed and one unannealed sample. The carbon content was measured at 0.01% before the annealing and 0.03% after the annealing, suggesting absorption of carbon by the surface of the samples during annealing. The penetration depth of the absorbed carbon and its effect on the magnetic properties of printed steel is planned for a future study. Significant grain growth was observed (Figure 4b) after the annealing process: the fine-grained microstructure recrystallized into a course-grained microstructure (D~500 µm). The as-built state shows columnar microstructure with a strong texture in the build direction resulting from epitaxial growth and steep temperature gradients in the build direction. Similar to [11], the epitaxial structure has disappeared in the annealed state; however, the coarse grains appear to have retained the elongated columnar structure in the build direction post-annealing.

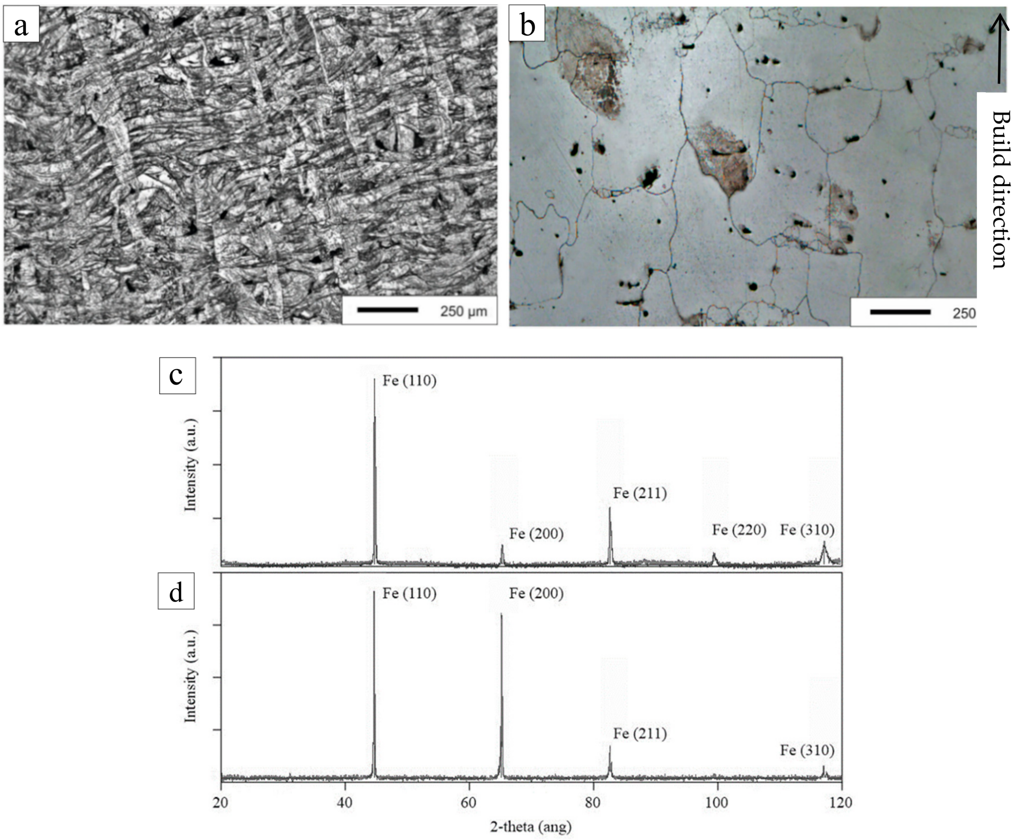

Figure 4. Optical micrographs of the printed material grain structure (**a**) before and (**b**) after annealing. XRD (X-ray diffraction) analysis of the printed toroid (**c**) before and (**d**) after annealing (measured from the cross-sectional plane of the toroid).

XRD (X-ray diffraction) analysis was performed to investigate the micro-phase distribution in as-built and annealed material. The XRD patterns suggest the evolution of the preferred orientation from ⟨1 1 0⟩ to ⟨1 0 0⟩ crystallization axis (easy magnetization [21]) in parallel to the magnetization direction in the recrystallized toroid. This indicates the capacity of recrystallized laser re-melted SLM structure to exhibit beneficial grain structure for magnetic applications, prompting future research.

2.5. Methods of Magnetic Measurements and Losses Segregation

In this study, the ring method was employed for the measurement of printed material magnetic properties. The measurements were conducted at frequencies of 25 mHz (quasi-static), 1, 10 and 50 Hz, in the magnetization range of 0.9–1.6 T. The measurements were completed in accordance with the European standard EN 60404-6 [22]. The quasi-static measurement methods agree with the EN 60404-4 standard [23]: employing continuous recording method with the toroid first demagnetized with gradually reducing the magnetic field and completing the magnetization cycle time in the range of 30–60 s. The drift correction of the measured induced voltage for DC measurements was performed similar to [24]. The schematic of the magnetic measurements setup is shown in Figure 5a. Dewetron DEWE2-M data acquisition system at 10 kHz sampling frequency was used for logging the induced voltage on the sensing coil and the voltage drop over the shunt precision resistor of 75 mV/15A in the primary coil circuit. In all experiments, sinusoidal excitation current was used. Signal Amplifer Omicron CMS 356 was used for amplifying the generated signal from the waveform generator and maintaining its sinusoidal waveform throughout the experiment. The magnetic field strength H was calculated by (1) and the average flux density by (2):

$$H = \frac{N_1 i}{l_t} \tag{1}$$

$$B = \frac{1}{N_2 S} \int_t e(t) dt \tag{2}$$

where N_1—is number of turns of the primary coil, N_2—the number of turns of the secondary coil, i—the instantaneous current value, e—the instantaneous induced electromotive force, l_t—the toroid average length and S—toroid cross-sectional area. After constructing the hysteresis curves from the measured data, the hysteresis curves were halved into two sets of data corresponding to the direction of the magnetizing force. Both halves were then fitted with cubic fitting splines for noise and data points reduction for simplifying the integration of the curves. The specific iron losses (P_s) were then found as a subtraction of the curve areas and accounting for the average density (ρ) and period (T) of each hysteresis cycle, as expressed in (3).

$$P_s = \frac{1}{T\rho}\left(\int_0^T H_1 dB_1 - \int_0^T H_2 dB_2\right) \tag{3}$$

Calculated total iron losses were then segregated into hysteresis, classical and excess eddy current losses for more accurate description of the printed material behavior. Hysteresis losses were calculated from the quasi-static measurements. For the estimation of eddy current losses in the printed material, FEM (finite element method) analysis was conducted, as the analytical means are insufficient for the calculation of generated eddy currents in the nonlaminated printed toroids. Eddy current losses were simulated in a commercial FE software Infolytica Magnet (Version v2020_1, Montreal, Canada). The model geometry imitated the experimental measurements of the toroid. Due to the physical nature of the eddy currents, three-dimensional transient analysis was conducted. The axial symmetry of the toroid favored the simulation of only a small part of the toroid in 3D (length 0.5 mm), with symmetric boundary conditions segregating the sector. The geometry and mesh of the model are shown in Figure 5b. The setup was modeled with a single coil, since the software enables the calculation of the flux linkage through it and a separate sensing coil is unnecessary. The model was excited with an undistorted AC current with RMS value altered until the desired maximum flux density B_{max} was achieved. Transient step size of a two hundredths of the excitation current period was used for simulating two current periods of each simulation. The magnetization curves of the FEM models were determined from the centerlines of the experimentally measured quasi-static hysteresis curves and the resistivity from the previously experimentally measured average value of 98 μΩ·cm.

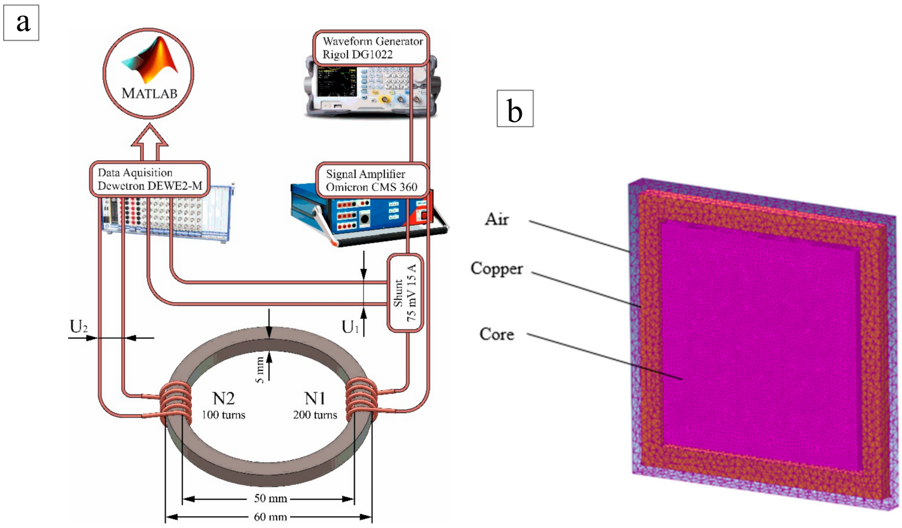

Figure 5. (**a**) Toroid dimensions and the schematic of the hysteresis measurements. (**b**) Geometry and mesh of the finite element method (FEM) simulation.

3. Results of Magnetic Measurements and Discussion

3.1. DC Properties

Quasi-static measurements of the sample presented in Figure 6 shows comparable DC magnetic properties to commercial and 3D printed soft ferromagnetic materials from the literature. The main drawback of the material characterized in this study is the relatively low saturation magnetization of 1.3 T (at 5000 A/m), compared to other commercial grade Non-Oriented Electrical Steels according to Standard EN 10106 of 1.6–1.7 T (at 5000 A/m). The reduced saturation magnetization can most likely be attributed to the pinning effect of intragranular porosities [25,26] on the large recrystallized grains.

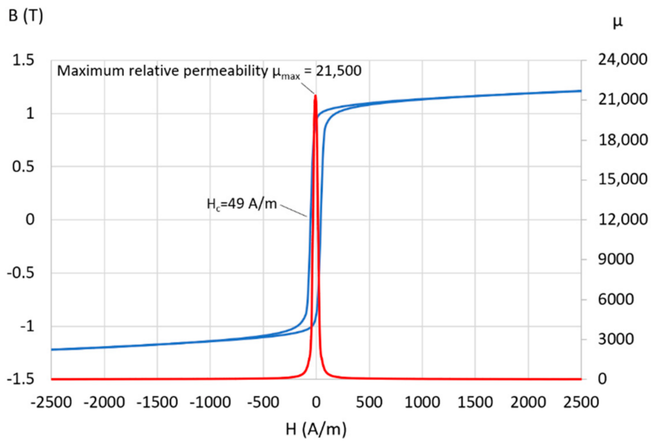

Figure 6. Quasi-static hysteresis curve and permeability of the toroid (annealed). Measured with sinusoidal excitation of 2500 A/m at 25 mHz.

For SLM-fabricated soft magnetic materials in the literature, DC relative permeability in the range of 25,000–31,000 [11,12] and coercivity of 16 A/m [11,12] for printed 6.7–6.9% silicon steel has been obtained. For the material characterized in this study, the slightly lower maximum permeability of

21,500 (at 2500 A/m) and higher coercivity of 49 A/m can most likely be attributed to impurity content (as described by Brissonneau in 1980 [27]) in the printed material (defect, chromium and carbon content). DC losses expressing the total hysteresis losses of the material printed in this study were calculated at 0.95 W/kg (at 1 T, 50 Hz) and 2.81 W/kg (at 1.5 T, 50 Hz). As a comparison, Garibaldi [12] has previously obtained a total power loss of 2.2 W/kg (1 T, 50 Hz) on annealed printed ring samples with a cross section of 2 × 4 mm (including limited eddy current losses component) and Goll [11] has calculated 0.7 W/kg hysteresis (1 T, 50 Hz) and approximately 6.5 W/kg (5 × 5 mm ring sample cross section) of total iron losses in her work with SLM-fabricated 6.7% silicon steel. For commercial grade non-oriented electrical steel sheets, total iron losses have been shown to range from 2.2–2.5 W/kg (Top grade, 2.5–3.2% Si, thickness 0.35–0.5 mm, 1.5 T, 50 Hz) to 7–9 W/kg (Low grade, 0.5–1.5% Si, thickness 0.5–0.65 mm, 1.5 T, 50 Hz) [27,28]. The total iron losses of 6.5% non-oriented silicon steel laminations are typically in the range of 0.5–0.7 W/kg (thickness 0.5 mm, 1 T, 50 Hz) [21] and Somaloy has been shown to exhibit total iron losses 6.6–10 W/kg (5 × 5 mm cross section, 1.5T, 50 Hz) [29].

3.2. AC Properties

Further measurements at higher frequencies and field strengths confirmed the substantial increase of the material coercivity and core losses accompanied by the decrease in its maximum permeability. As the samples exhibit 5 × 5 mm bulk cross-sectional area, significant eddy currents are induced, which are responsible for the majority of hysteresis curve shearing and growth of its area. The shearing effect is visualized in Figure 7, presenting the measured hysteresis curves at 50 Hz in the magnetization range of 1–1.5 T, alongside the calculated total iron loss for each curve.

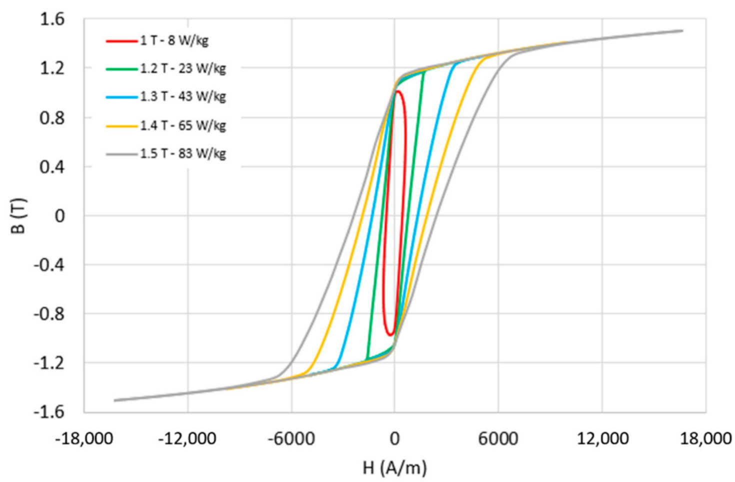

Figure 7. Hysteresis curves measured at 50 Hz in the magnetization range of 1–1.5 T (annealed).

The behavior of sample relative magnetic permeability and coercivity are shown in Figure 8 in the range of 1.1 to 1.5 T at 1, 10 and 50 Hz. The highest maximum relative AC permeability μ_{max} in the study was measured at 10,850 (1.11 T, 1 Hz) post-annealing, which decreased to 2200 (1.5 T, 1 Hz) and was further reduced to 200 at higher excitation frequency (1.5 T, 50 Hz).

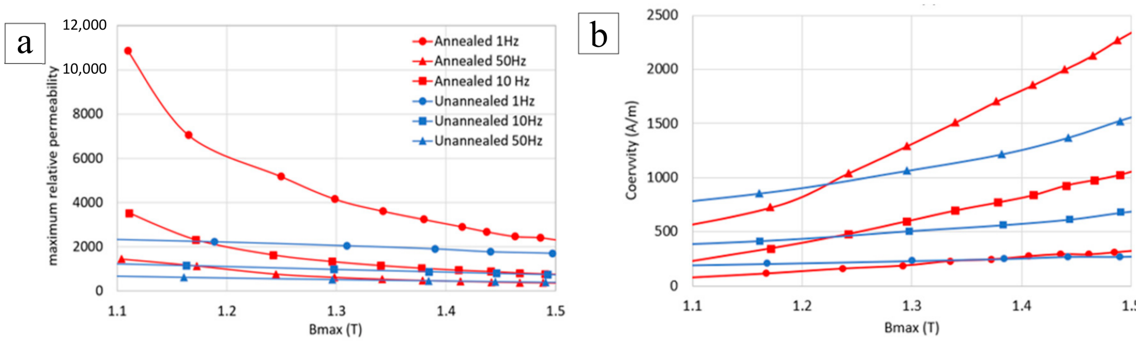

Figure 8. Measured (**a**) maximum relative permeability and (**b**) coercivity of the toroid before and after annealing at 1, 10 and 50 Hz, in the magnetization range of 1.1 to 1.5 T.

The unannealed sample exhibited considerably lower μ_{max} of 2400 (1 T, 1 Hz), 1650 (1.5 T, 1 Hz) and 380 (1.5 T, 50 Hz). Coercivity of the samples ranged from 87 A/m (1.08 T, 1 Hz) post-annealing, which increased to 334 A/m (1.5 T, 1 Hz) and was further increased to 2400 A/m at higher excitation frequency (1.5 T, 50 Hz). Both the material coercivity and total iron losses increased roughly above the knee point of the material over all measured frequencies after the annealing process. Calculated iron losses in the magnetization range of 0.9–1.5 T at 1, 10 and 50 Hz are presented Figure 8. The summary of the iron losses is presented in Table 3 with the losses ranging from 83.7 W/kg (Annealed, 1.5 T, 50 Hz) to 0.022 W/kg (Annealed, 1 T, 1 Hz).

Table 3. Iron losses at 1, 10, and 50 Hz.

Sample	1 Hz (W/kg)	10 Hz (W/kg)	50 Hz (W/kg)
Annealed, 1 T	0.022	0.60	8.17
Unannealed, 1 T	0.077	1.37	14.17
Annealed, 1.5 T	0.23	7.1	83.7
Unannealed, 1.5 T	0.16	3.5	47.3

The total iron losses decreased after the annealing at 1 T magnetization, however increased at 1.5 T over all the measured frequencies. Loss segregation was performed for clarification of the loss behavior through the subtraction of hysteresis (obtained through quasi-static measurements) and eddy current losses (obtained through simulation) from the total measured losses. Eddy currents were identified as the main component of the measured losses, generated due to the unlaminated, fully dense cross section of the sample toroid. FEM analysis of the toroid cross section correlated with the losses measured: comparison of the simulated hysteresis curve expressing only the FEM eddy current losses and the measured total losses at 1.5 T, 50 Hz is shown in Figure 9. The difference of the area between the hysteresis curves presented in Figure 10 represents the sum of hysteresis and excess eddy current losses. The area of the hysteresis curves was then used for the calculation of hysteresis losses. Excess eddy currents are not calculated and are obtained from the segregation. Table 4 presents the segregated losses of both the annealed and unannealed samples at 1 and 1.5 T.

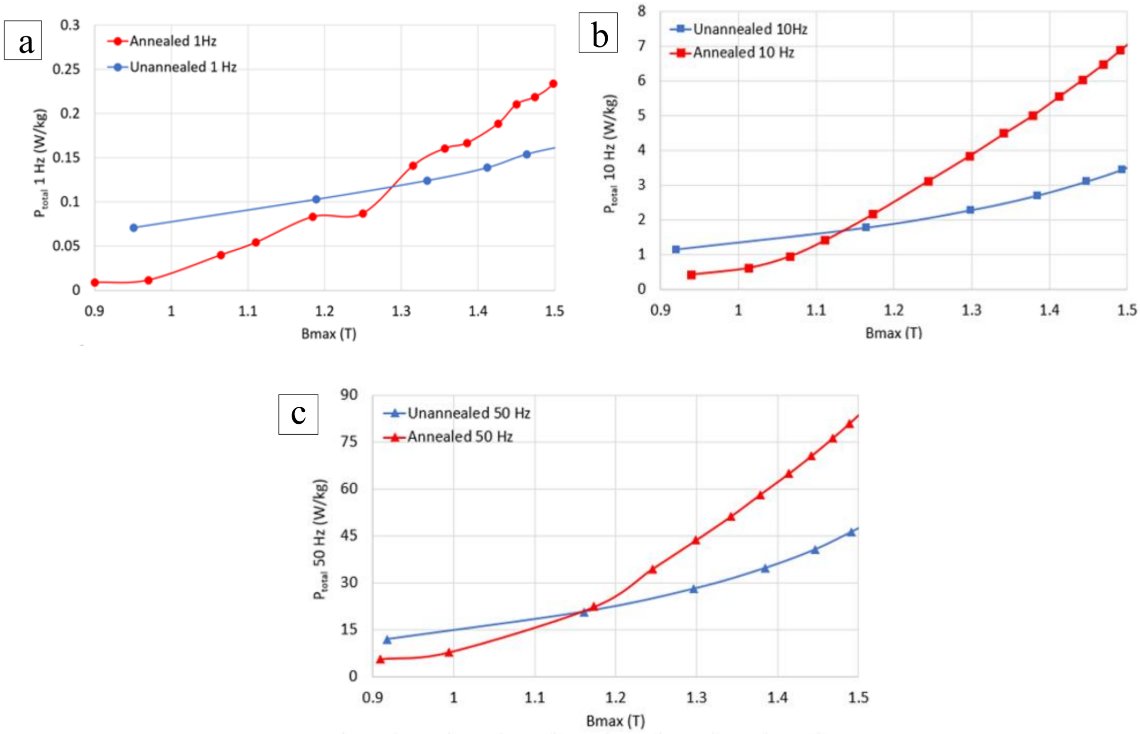

Figure 9. Total iron losses as a function of magnetization of both the annealed and unannealed toroid in the magnetization range of ~0.9–1.5 T: (**a**) 1 Hz, (**b**) 10 Hz and (**c**) 50 Hz.

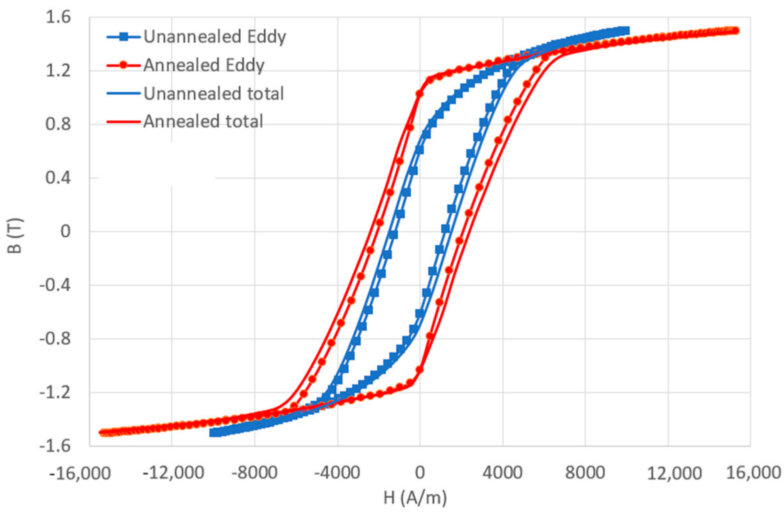

Figure 10. Comparison of simulated eddy current losses and total iron losses at 1.5 T, 50 Hz before and after annealing.

Table 4. Segregated iron losses at 50 Hz.

Sample	Total (W/kg)	Hysteresis (W/kg)	Eddy (W/kg)	Excess (W/kg)
Annealed, 1 T	8.17	0.95	6.26	0.96
Unannealed, 1 T	14.17	3.65	7.85	2.67
Annealed, 1.5 T	83.7	2.81	74.3	6.59
Unannealed, 1.5 T	47.3	7.18	37.6	2.52

The hysteresis loss reduction after annealing is well documented [28,30] and can mostly be attributed to the material grain growth and the relief of internal stress. The segregated losses confirm the reduction of hysteresis losses after the annealing process: dropping by 74% at 1T and 61% at 1.5 T. In general, the classical eddy current losses are shown to increase after annealing [31]. In this study the eddy current losses however decreased by 20% at 1 T and approximately doubled in magnitude at 1.5 T after the annealing process. The authors propose the effect of nonlinear saturation losses to explain for this phenomenon. Presently, formation of eddy currents in silicon steel has widely been studied and modelled mostly for laminated structures and for non-saturated conditions, complicating comparisons with an analytical model (such as the Bertotti model) [32]. In deep saturation, a new loss component of nonlinear saturation losses should be considered in addition to the classical loss components of hysteresis, classical Foucault eddy current and excess eddy current losses [33–36]. This loss component would help to explain the decrease in eddy current loss at 1 T (annealed sample not saturated) and the increase at 1.5 T (both saturated, but the annealed sample magnetized at 1.5 T at considerably higher magnetic field strength) after the annealing process.

Excess losses can be related to the microscopic eddy currents arising from the domain wall motion, and they have been shown to increase with domain (also grain) size [37]. In this study, as the segregated excess losses were not calculated separately, they incorporate the eddy and hysteresis losses calculation error as well. The classical eddy current error of calculation can mostly be the result of inhomogeneous resistivity of the material due to internal cracking and porosities, which complicates accurate estimation of the eddy current generation in the entirety of the toroid in the FEM simulation. The proportion of the post-annealed excess loss can be considerably more from the estimation, due to extensive grain growth and underestimated resistivity of the cross-section of the toroid (due to porosities and cracks present in the printed material).

Despite limitations however, the segregation process gave a rough estimation on the magnitude and contribution of each of the loss type on the total losses, confirmed by extensive Foucault eddy current losses in the printed bulk material and suggesting next steps for the reduction of iron losses in the printed material. Additionally, the determination of the behavior of each loss component in saturated state is planned as future work due to its significant impact on 3D printed material performance, especially with the potential material oversaturation due to the reduced filling factor in partitioned material designs discussed in the next chapter.

4. Future Work

Selective laser melting (SLM) technology is currently unsuitable for eddy current reduction via laminated structure due to complications in printing multiple materials in parallel with different thermal behavior and due the powder bed-based nature of the process, enabling the usage of a single powder concurrently. Recent breakthroughs in powder deposition, enabling the selective powder deposition of multiple materials [38], suggests that in the near future, multi-material SLM printing of electromechanical components might be available. Presently, it can be suggested that eddy current losses can be reduced in printed components by geometrical manipulation: printing of materials with refined internal structures. The evolution of material can be accomplished by introducing air gaps to the material perpendicular to the flux direction or printing the material as a dense lattice structure. For the verification of eddy current reduction with geometrical manipulation, FEM analysis was performed on a slotted toroidal part with cross-section geometry as shown in Figure 11 alongside the FEM simulated current density J in the toroidal cross-section. The proposed geometry in the current study was chosen arbitrarily to illustrate the effectiveness of printed air gaps in the magnetic material for eddy current reduction and will require further optimization.

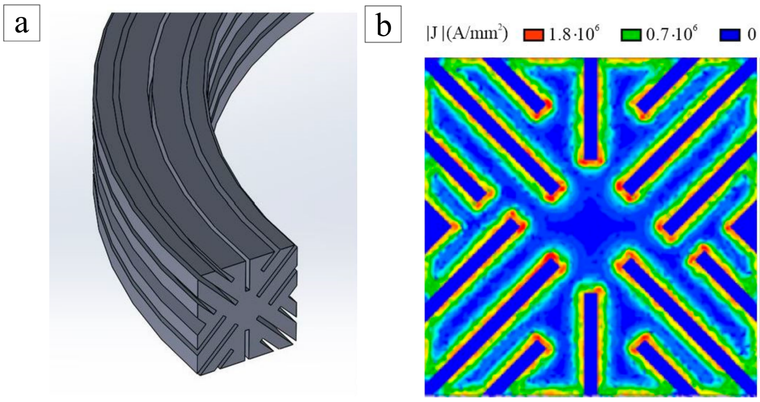

Figure 11. (**a**) Modeled toroid geometry, (**b**) Simulated induced current density in the toroid cross section at time moment field zero-crossing (H = 0).

Eddy current losses were again calculated from the obtained hysteresis curves, presented in Figure 12. The eddy current loss decreased from 75.3 to 10.9 W/kg (decrease of 85%) when calculating the hysteresis loops according to the true area of the slotted cross section. When taking into account, however, the full area occupied by the geometry (solid area), the average magnetic flux density across the cross-section also reduces from 1.5 to 1.2 T, suggesting a tradeoff between eddy current loss reduction through geometry manipulation and maximum flux density obtained in the soft ferromagnetic part. The air content and the filling factor of the magnetic material in the manipulated part would then dependent on the spatial manufacturing accuracy of the printing system in question. Optimally, the cross-sectional area should be as dense as possible for achieving high saturation magnetization and as partitioned as realizable for limiting the induced eddy currents while retaining the mechanical strength required by its application. Presently, state-of-the-art slotted geometry with an average relative density of 56.5% with Hilbert curve structure has been used in [13] for obtaining near fully decayed eddy currents in printed material. Lattice structures have been shown to exhibit excellent strength to weight mechanical properties for different alloys [39,40], however have not undergone experimental or FEM magnetic property analysis in the literature. Additionally, lattice structures show even more reduced filling factor in the range of 30–40% [41].

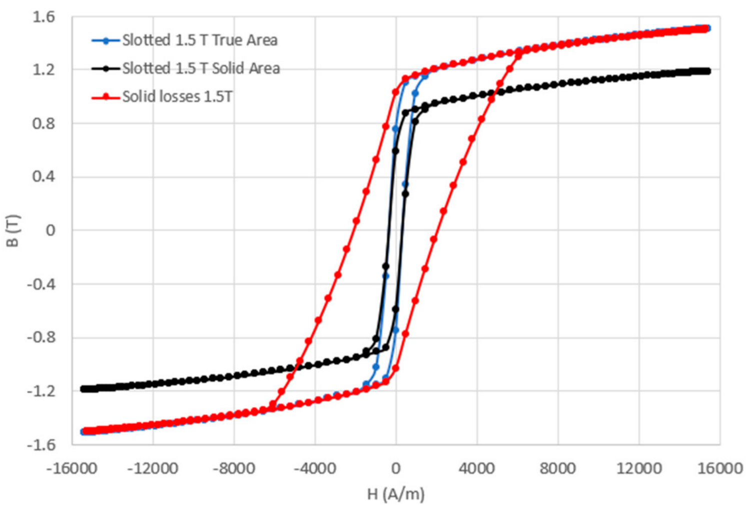

Figure 12. Hysteresis curve comparison between the modelled solid material, slotted model calculated with true area and slotted model calculated with the solid cross-sectional area.

5. Conclusions

The paper described the sample preparation and hysteresis measurements of SLM-processed ring samples. The powder employed for manufacturing contained approximately 94.7% Fe, 4% Si and 1.3% Cr. Quasi-static measurements revealed comparable DC magnetic properties to commercial and other additively manufactured soft ferromagnetic materials with DC hysteresis losses of 0.95 W/kg (1 T, 50 Hz) and 2.81 W/kg (1.5 T, 50 Hz). Despite beneficial grain orientation, the sample in the study showed lower saturation magnetization when compared to other commercial electrical steels, most likely due to the pinning effect of intragranular porosities on the large recrystallized grains.

AC measurements demonstrated a considerable increase in measured iron losses, which were confirmed as predominantly classical eddy current losses. The losses were also shown to intensify in deep saturation of the material: increasing from 8.17 (1 T) to 83.7 W/kg (1.5 T) for the ring sample after the annealing, suggesting the nonlinear saturation core losses component at magnetization in deep saturation. Both empirical and FEM results confirm considerable eddy currents generated in the printed bulk toroidal sample, which increase dramatically at high material saturation. Geometrical manipulation was proposed as a promising method for classical eddy current losses reduction, however potentially resulting in a poor filling factor and thus lower magnetic saturation of the magnetic material. This would result in:

Substantially increased iron and copper losses if the operation point of the magnetic material is shifted into the nonlinear part of the magnetization curve to compensate for the reduced filling factor; and

Operating the magnetic material below its optimal knee point, resulting in reduced flux density in the ferromagnetic component.

Future research of the project will involve the optimization of the material filling factor and structure for minimal iron losses and maximum flux density conducted in the material with considerations to its mechanical properties.

Author Contributions: Conceptualization: A.K.; Methodology: A.R.; Validation, D.L.; Investigation, H.T.; Resources, H.T.; Writing—original draft preparation, H.T.; Writing—review and editing, H.T., A.K., A.B.; Supervision, A.K., A.B. A.R., D.L.; Project Administration, T.V.; Funding acquisition, A.K. All authors have read and agreed to the published version of the manuscript.

Funding: This research work was funded by Estonian Ministry of Education and Research (Grant PSG-137) and Government of Russian Federation (Grant 08-08). The APC was funded by Estonian Ministry of Education and Research, grant PSG-137.

Acknowledgments: Preparation of micrograph samples, SEM and EDX analyses were supported by the projects IUT-19-28 and TK-141.

Conflicts of Interest: The authors declare no conflict of interest.

References

1. Lammers, S.; Adam, G.; Schmid, H.-J.; Mrozek, R.; Oberacker, R.; Hoffmann, M.J.; Quattrone, F.; Ponick, B. Additive Manufacturing of a lightweight rotor for a permanent magnet synchronous machine. In Proceedings of the 2016 6th International Electric Drives Production Conference (EDPC), Nuremberg, Germany, 30 November–1 December 2016; Institute of Electrical and Electronics Engineers (IEEE): Nuremberg, Germany, 2016; Volume 13, pp. 41–45.
2. Zhang, Z.-Y.; Jhong, K.J.; Cheng, C.-W.; Huang, P.-W.; Tsai, M.-C.; Lee, W.-H. Metal 3D printing of synchronous reluctance motor. In Proceedings of the 2016 IEEE International Conference on Industrial Technology (ICIT), Taipei, Taiwan, 14–17 March 2016; Institute of Electrical and Electronics Engineers (IEEE): Taipei, Taiwan, 2016; pp. 1125–1128.
3. Rassõlkin, A.; Kallaste, A.; Vaimann, T.; Tiismus, H. Control Challenges of 3D Printed Switched Reluctance Motor. In Proceedings of the 2019 26th International Workshop on Electric Drives: Improvement in Efficiency of Electric Drives (IWED), Moscow, Russia, 30 January–2 February 2019; Volume 1, pp. 1–5. [CrossRef]

4. Simpson, N.; Mellor, P. Additive manufacturing of shaped profile windings for minimal AC loss in gapped inductors. In Proceedings of the 2017 IEEE International Electric Machines and Drives Conference (IEMDC), Miami, FL, USA, 21–24 May 2017; pp. 1–7. [CrossRef]
5. Lorenz, F.; Rudolph, J.; Wemer, R. Design of 3D Printed High Performance Windings for Switched Reluctance Machines. In Proceedings of the 2018 XIII International Conference on Electrical Machines (ICEM), Alexandroupoli, Greece, 3–6 September 2018; pp. 2451–2457. [CrossRef]
6. Tate, J.G.; Richardson, B.; Love, L. *Additive Manufacturing for Low Volume Bearings*; Office of Scientific and Technical Information (OSTI): Oak Ridge, TN, USA, 2017.
7. Aguilera, E.; Ramos, J.; Espalin, D.; Cedillos, F.; Muse, D.; Wicker, R.; MacDonald, E. 3D printing of electro mechanical systems. In Proceedings of the 24th Annual International Solid Freeform Fabrication Symposium: An Additive Manufacturing Conference, University of Texas at Austin, TX, USA, 12–14 August 2013; pp. 950–961.
8. Tiismus, H.; Kallaste, A.; Vaimann, T.; Rassolkin, A.; Belahcen, A. Technologies for Additive Manufacturing of Electrical Machines. In Proceedings of the 2019 20th International Conference of Young Specialists on Micro/Nanotechnologies and Electron Devices (EDM), Erlagol (Altai Republic), Russia, 29 June–3 July 2019; pp. 651–655. [CrossRef]
9. Silbernagel, C.; Gargalis, L.; Ashcroft, I.; Hague, R.; Galea, M.; Dickens, P. Electrical resistivity of pure copper processed by medium-powered laser powder bed fusion additive manufacturing for use in electromagnetic applications. *Addit. Manuf.* **2019**, *29*, 100831. [CrossRef]
10. Silbernagel, C.; Ashcroft, I.; Dickens, P.; Galea, M. Electrical resistivity of additively manufactured AlSi10Mg for use in electric motors. *Addit. Manuf.* **2018**, *21*, 395–403. [CrossRef]
11. Goll, D.; Schuller, D.; Martinek, G.; Kunert, T.; Schurr, J.; Sinz, C.; Schubert, T.; Bernthaler, T.; Riegel, H.; Schneider, G. Additive manufacturing of soft magnetic materials and components. *Addit. Manuf.* **2019**, *27*, 428–439. [CrossRef]
12. Garibaldi, M.; Ashcroft, I.; Lemke, J.; Simonelli, M.; Hague, R. Effect of annealing on the microstructure and magnetic properties of soft magnetic Fe-Si produced via laser additive manufacturing. *Scr. Mater.* **2018**, *142*, 121–125. [CrossRef]
13. Plotkowski, A.; Pries, J.; List, F.; Nandwana, P.; Stump, B.; Carver, K.; Dehoff, R. Influence of scan pattern and geometry on the microstructure and soft-magnetic performance of additively manufactured Fe-Si. *Addit. Manuf.* **2019**, *29*, 100781. [CrossRef]
14. Riipinen, T.; Metsä-Kortelainen, S.; Lindroos, T.; Keränen, J.; Manninen, A.; Pippuri-Makelainen, J. Properties of soft magnetic Fe-Co-V alloy produced by laser powder bed fusion. *Rapid Prototyp. J.* **2019**, *25*, 699–707. [CrossRef]
15. Kang, N.; El Mansori, M.; Guittonneau, F.; Liao, H.; Fu, Y.; Aubry, E. Controllable mesostructure, magnetic properties of soft magnetic Fe-Ni-Si by using selective laser melting from nickel coated high silicon steel powder. *Appl. Surf. Sci.* **2018**, *455*, 736–741. [CrossRef]
16. Chen, W.; Liu, J.; Cheng, Z.; Lin, X.; Zhu, J. Effect of Chromium on Microstructure, Ordered Phase and Magnetic Properties of Fe-6.5 wt%Si Alloy. *Mater. Today: Proc.* **2015**, *2*, S314–S318. [CrossRef]
17. Oxley, P.; Goodell, J., Jr.; Molt, R. Magnetic properties of stainless steels at room and cryogenic temperatures. *J. Magn. Magn. Mater.* **2009**, *321*, 2107–2114. [CrossRef]
18. Yasa, E.; Deckers, J.; Kruth, J.-P. The investigation of the influence of laser re-melting on density, surface quality and microstructure of selective laser melting parts. *Rapid Prototyp. J.* **2011**, *17*, 312–327. [CrossRef]
19. Yang, X.; Liu, J.; Cui, X.; Jin, G.; Liu, Z.; Chen, Y.; Feng, X. Effect of remelting on microstructure and magnetic properties of Fe-Co-based alloys produced by laser additive manufacturing. *J. Phys. Chem. Solids* **2019**, *130*, 210–216. [CrossRef]
20. Liu, B.; Li, B.-Q.; Li, Z. Selective laser remelting of an additive layer manufacturing process on AlSi10Mg. *Results Phys.* **2019**, *12*, 982–988. [CrossRef]
21. Ouyang, G.; Chen, X.; Liang, Y.; Macziewski, C.; Cui, J. Review of Fe-6.5 wt%Si high silicon steel—A promising soft magnetic material for sub-kHz application. *J. Magn. Magn. Mater.* **2019**, *481*, 234–250. [CrossRef]

22. European Committee for Electrotechnical Standardization. *European Standard EN 60404-6: Magnetic Materials—Part 6: Methods of Measurement of the Magnetic Properties of Magnetically Soft Metallic and Powder Materials at Frequencies in the Range 20 Hz to 100 kHz by the Use of Ring Specimens*; International Electrotechnical Commission: Geneva, Switzerland, 2004; TC-68. Available online: http://www.evs.ee/et/iec-60404-6-2018 (accessed on 9 June 2020).
23. European Committee for Electrotechnical Standardization. *European Standard EN 60404-4: Magnetic Materials—Part 4: Methods of Measurement of d.c. Magnetic Properties of Iron and Steel*; International Electrotechnical Commission: Geneva, Switzerland, 2002; TC-68. Available online: http://www.evs.ee/et/evs-en-60404-4-2002-a2-2009 (accessed on 9 June 2020).
24. Garcia, J.; Rivas, M. A quasi-static magnetic hysteresis loop measurement system with drift correction. *IEEE Trans. Magn.* **2005**, *42*, 15–17. [CrossRef]
25. Goldman, A. *Handbook of Modern Ferromagnetic Materials*; Springer Science and Business Media LLC: Pittsburgh, PA, USA, 1999.
26. Globus, A.I. Magnetization Mechanisms Some Physical Considerations About the Domain Wall Size Theory of Magnetization Mechanisms. *J. Phys. Colloq.* **1977**, *38*, C1. [CrossRef]
27. Brissonneau, P. Non-oriented Si-Fe Sheets. *J. Magn. Magn. Mater.* **1980**, *19*, 52–59. [CrossRef]
28. Tumanski, S. *Handbook of Magnetic Measurements*; CRC Press: Boca Raton, FL, USA, 2016.
29. Hoganas. Material Data: Somaloy. Available online: http://www.hoganas.com/electromagnetic (accessed on 9 June 2020).
30. Shimanaka, H.; Ito, Y.; Matsumara, K.; Fukuda, B. Recent development of non-oriented electrical steel sheets. *J. Magn. Magn. Mater.* **1982**, *26*, 57–64. [CrossRef]
31. Almeida, A.A.; Rodrigues, D.L., Jr.; Perassa, L.S.P.; Leicht, J.; Landgraf, F.J.G. Anomalous loss hysteresis loop. *Mater. Res.* **2014**, *17*, 494–497. [CrossRef]
32. Krings, A.; Soulard, J. Overview and Comparison of Iron Loss Models for Electrical Machines. *J. Electr. Eng.* **2010**, *10*, 162–169.
33. Eggers, D.; Steentjes, S.; Hameyer, K. Advanced Iron-Loss Estimation for Nonlinear Material Behavior. *IEEE Trans. Magn.* **2012**, *48*, 3021–3024. [CrossRef]
34. Steentjes, S.; Leßmann, M.; Hameyer, K. Semi-physical parameter identification for an iron-loss formula allowing loss-separation. *J. Appl. Phys.* **2013**, *113*, 17A319. [CrossRef]
35. Elfgen, S.; Franck, D.; Hameyer, K. Characterisation of soft magnetic materials by measurement: Evaluation of uncertainties up to 1.8 T and 9 kHz. *AIP Adv.* **2018**, *8*, 47208. [CrossRef]
36. Karthaus, J.; Steentjes, S.; Leuning, N.; Hameyer, K. Effect of mechanical stress on different iron loss components up to high frequencies and magnetic flux densities. *COMPEL Int. J. Comput. Math. Electr. Electron. Eng.* **2017**, *36*, 580–592. [CrossRef]
37. Oda, Y.; Okubo, T.; Takata, M. *Recent Development of Non-Oriented Electrical Steel in JFE Steel*; Techical Report for JFE. Rep., 21; JFE Steel Corporation: Kawasaki, Japan, 2016; pp. 7–13.
38. Aerosint. Selective Powder Deposition for AM. Available online: https://aerosint.com/ (accessed on 11 June 2020).
39. Gangireddy, S.; Komarasamy, M.; Faierson, E.J.; Mishra, R.S. High strain rate mechanical behavior of Ti-6Al-4V octet lattice structures additively manufactured by selective laser melting (SLM). *Mater. Sci. Eng. A* **2019**, *745*, 231–239. [CrossRef]
40. Leary, M.; Mazur, M.; Williams, H.; Yang, E.; Alghamdi, A.; Lozanovski, B.; Zhang, X.; Shidid, D.; Farahbod-Sternahl, L.; Witt, G.; et al. Inconel 625 lattice structures manufactured by selective laser melting (SLM): Mechanical properties, deformation and failure modes. *Mater. Des.* **2018**, *157*, 179–199. [CrossRef]
41. Maconachie, T.; Leary, M.; Lozanovski, B.; Zhang, X.; Qian, M.; Faruque, O.; Brandt, M.; Zhang, X. SLM lattice structures: Properties, performance, applications and challenges. *Mater. Des.* **2019**, *183*, 108137. [CrossRef]